Continuous-Wave Nonlinear Polarization Control and Signatures of Criticality in a Perovskite Cavity

G. Keijsers,[1] R. M. de Boer,[1] B. Verdonschot,[1] K. J. H. Peters,[1] Z. Geng,[1] and S. R. K. Rodriguez[1,*]

[1] *Center for Nanophotonics, AMOLF, Science Park 104, 1098 XG Amsterdam, The Netherlands*

(Dated: November 28, 2024)

Halide perovskites have emerged as promising photonic materials for fundamental physics studies and technological applications. Their potential for nonlinear optics has also drawn great interest recently; yet, to date, continuous-wave (CW) nonlinearities have remained elusive. Here we demonstrate CW nonlinear phenomena in a $CsPbBr_3$ perovskite cavity. We first demonstrate optical bistability — the hallmark of single-mode coherent nonlinear optics. Next we exploit the interplay of nonlinearity and birefringence to demonstrate nonlinear control over the polarization of light. Finally, by measuring the optical hysteresis of our cavity as a function of temperature, we find a dramatic enhancement of the nonlinearity around 65 K. This enhancement is indicative of a phase transition in $CsPbBr_3$. Our results position $CsPbBr_3$ cavities as an exceptional platform for nonlinear optics, offering strong CW nonlinearity and birefringence which are furthermore tunable. Moreover, our approach to uncover signatures of a phase transition of matter via optical hysteresis measurements is promising for exploring strongly correlated states of light-matter systems.

Halide perovskites (HP) have inspired major research developments in optoelectronics [1] and photonics [2, 3] over the past decade. Among their many interesting features, HPs host large-binding-energy excitons suitable for strong coupling to optical modes at room temperature [4]. This strong coupling results in part-light part-matter quasi-particles known as polaritons, which can interact via their exciton part and enhance optical nonlinearities [5]. Experiments under non-resonant or pulsed excitation have revealed nonlinear phenomena such as condensation [6–9], optical switching [10, 11], parametric scattering [12, 13], and superfluidity [14] of polaritons in HPs. However, under coherent CW driving, HPs typically bleach at power densities below nonlinear thresholds.

Among the various nonlinear effects pursued with HPs [15] and other emergent materials [16], those involving an intensity-dependent refractive index rank highly. The Kerr effect, for example, involves an instantaneous refractive index change and is key to fascinating phenomena such as superfluidity [17], photon blockade [18], and nonlinear polarization control [19, 20]. The related thermo-optical nonlinearity, which involves a non-instantaneous refractive index change, has recently drawn interest for optical switching and isolation [21, 22]. In polariton systems, polariton-polariton interactions mediate Kerr nonlinearities [17], while polariton-exciton interactions yield a non-instantaneous refractive index change [23, 24]. Regardless of the nonlinear response time, CW operation is crucial for many fundamental studies and applications. Otherwise, a steady state cannot be reached and functionalities are limited. Imagine, for example, an optical memory with a lifetime that is as short as the sub-picosecond pulse pumping it, or an isolator that burns if the incident light is CW or pulsed with a repetition rate exceeding the cooling rate (typically MHz) of its constituent materials.

In this work we demonstrate CW nonlinear phenomena in a $CsPbBr_3$ perovskite polariton cavity. Our experiments, at 5 K, evidence optical bistability when probing a single mode, and signatures of tristability when probing two orthogonally-polarized modes nonlinearly coupled. Leveraging the nonlinearity of the two-mode system, we demonstrate full polarization rotation by controlling the laser-cavity detuning. We furthermore explore the temperature-dependent optical hysteresis of our cavity. Our experiments reveal a dramatic enhancement of the nonlinearity strength around 65 K, indicative of a phase transition in $CsPbBr_3$.

Results

Tunable birefringent perovskite cavity

Figure 1(a) illustrates our system: a tunable Fabry-Pérot microcavity hosting a $CsPbBr_3$ perovskite semiconductor, all inside a closed-cycle cryostat. The cavity is made by two distributed Bragg reflector (DBR) mirrors, each mounted on four piezoelectric actuators controlling their position and orientation. The bottom mirror supports $CsPbBr_3$ crystals, synthesized via chemical vapor deposition [25] and transferred onto the mirror using thermal release tape. The top mirror has several concave features (see Methods for details), each enabling us to make a plano-concave microcavity. Figure 1(b) shows a white-light transmission image of our cavity. Further details about our setup are reported in Methods and Supplementary Figure S1.

We first discuss the linear optics of our system when the perovskite crystal is far from all concave features and effectively embedded in a planar cavity. Figure 1(c) shows white light transmission spectra versus cavity length. For each longitudinal mode we observe two resonances, one vertically and the other horizontally polarized. The vertical (V) and horizontal (H) polarization axes are aligned with the slow and fast in-plane crys-

* s.rodriguez@amolf.nl

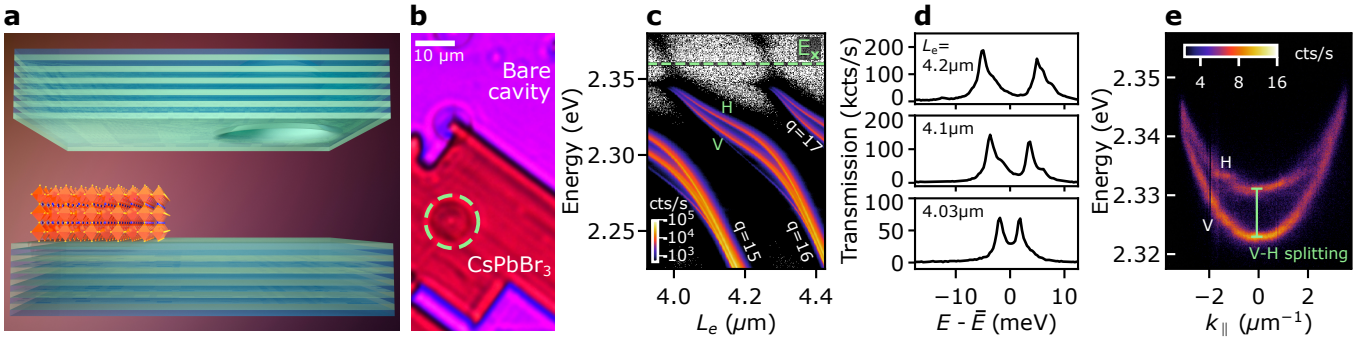

FIG. 1. **Tunable birefringent perovskite cavity.** (a) Sketch of the system under study: A cavity made by two DBR mirrors and hosting a $CsPbBr_3$ perovskite crystal. We switch between a planar and a plano-concave cavity by translating the top mirror, which contains a micron-scale concave mirror. (b) White light transmission image showing the $CsPbBr_3$ crystal in red, empty regions of the cavity in pink, and a concave mirror enclosed by the dashed circle. (c) Measured white light transmission spectrum of the planar cavity, as a function of the effective cavity length L_e. The modes are split in energy due to the birefringence of $CsPbBr_3$. The dashed green line indicates the exciton energy. (d) White light transmission spectra evidencing a widely tunable V-H splitting via the effective cavity length. (e) Momentum-resolved photoluminescence spectrum. Vertically and horizontally polarized lower polariton bands are labeled 'V' and 'H', respectively. For the measurements in (c,d,e), the $CsPbBr_3$ crystal is effectively embedded in a planar cavity.

talline axes, respectively. The frequency difference between orthogonally polarized modes is determined by the $CsPbBr_3$ birefringence, due to the orthorhombic crystal structure of $CsPbBr_3$ at low temperature [7, 8]. In Supplementary Figure S2 we present transfer-matrix calculations reproducing our experimental observations and confirming our interpretation. Calculations as a function of the perovskite crystal thickness in Supplementary Figure S3 further demonstrate that, for the crystal in our experiments, the observed resonances correspond to exciton-polaritons due to strong exciton-photon coupling.

Figure 1(c) illustrates how the V-H splitting can be tuned via the cavity length. Cuts at three distinct cavity lengths are presented in Figure 1(d). The largest V-H splitting observed, 10.4 meV, is 300-500 times greater than in GaAs cavities [19, 26]. Figure 1(e) illustrates the V-H splitting in momentum-resolved photoluminescence spectra measured at a fixed cavity length. The two emission bands with different dispersion relation have mutually orthogonal polarization. The bands cross at the largest in-plane momentum we can measure with our microscope objective. Similar band crossings, known as diabolic points, have recently drawn interest in connection to photonic realizations of non-Abelian gauge fields [27], Rashba-Dresselhaus Hamiltonians [28–30], and the quantum geometric tensor [31, 32]. However, experiments have remained limited by the lack of a system combining strong birefringence and continuous wave nonlinearity. Our system achieves that combination, with the added value of tunability in the birefringence (Fig. 1(c,d)) and the nonlinearity (shown ahead).

CW nonlinearity

We now switch to a plano-concave cavity configuration, enabling us to probe CW nonlinearities of single and coupled modes. To this end, we placed a concave feature above the $CsPbBr_3$ crystal and along the optical axis. The concave mirror discretizes the cavity spectrum: There is a finite number of transverse modes per longitudinal mode. In addition, the power needed for nonlinear effects is reduced because of the smaller mode volume. We drive the cavity with a single-mode 532 nm CW laser, and measure the polarization-resolved transmission as illustrated in Fig. 2(a). As a stepping stone, Fig. 2(b) shows transmission spectra for a relatively weak laser power 100 μW ensuring linear response. The incident light is diagonally polarized, thereby exciting both V and H polarized transverse cavity modes. The frequency difference between consecutive transverse cavity modes is determined by the radius of curvature of the concave mirror.

Figure 2(b) contains two insets showing how the transmitted intensity profiles resemble atomic orbitals. We label the resonances by their angular momentum number ℓ. Notice the proximity of the $\ell = 0$ H-polarized and $\ell = 2$ V-polarized resonances, characterized by 's'- and 'd'-like mode profiles, respectively. Their proximity is due to the $CsPbBr_3$ birefringence, which shifts V and H resonances as illustrated in the Fig. 2(b) top inset. In an empty cavity without $CsPbBr_3$, these two resonances would be highly detuned since H and V-polarized resonances with the same ℓ are degenerate. Imperfect concave mirrors with ellipticity can lift the degeneracy, but we do not observe this effect with the concave mirror under study and with our measurement resolution.

Figure 2(c) shows transmission spectra around the $\ell = 0$ H-polarized resonance for three distinct laser powers P. Spectra are referenced to the linear resonance linewidth Γ. The incident light is H polarized, excluding the excitation of V-polarized resonances. Solid

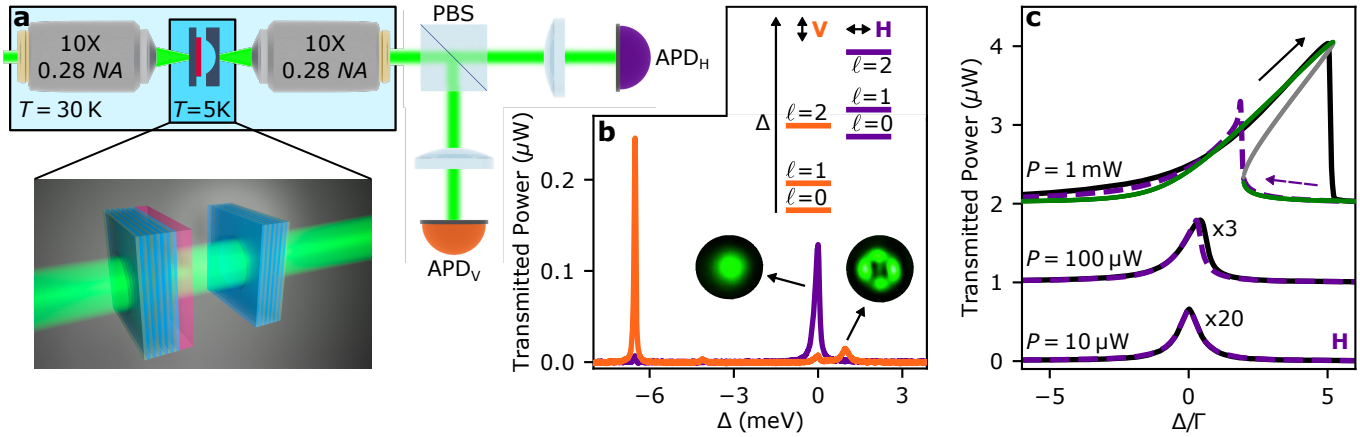

FIG. 2. **Polarization modes and optical bistability.** (a) Sketch of the setup used to obtain all results in Figures 2, 3, and 4 : A laser-driven tunable plano-concave microcavity containing a $CsPbBr_3$ crystal, all in a closed-cycle cryostat. The polarization-resolved transmitted power is measured using a polarizing beam splitter (PBS) and avalanche photodetectors APD_H and APD_V. (b) Orange and purple curves are transmitted powers collected in V and H polarization, respectively. The incident laser is diagonally polarized. Its $P = 100$ μW power is sufficiently low to ensure linear response. Δ is the frequency detuning between the laser and the $\ell = 0$ H-polarized resonance, which we control by scanning the cavity length. The spectrum is independent of scanning direction in this linear regime. Top inset: Schematic of the first three energy levels (transverse cavity modes) for each polarization, labeled with their angular momentum number ℓ. Side insets: Measured transmitted intensity profiles at the indicated resonances. (c) Solid black and dashed purple curves are the transmitted power, averaged over 70 cycles, when scanning Δ forward and backward, respectively. P is the laser power. Unlike in (b), here the incident laser is horizontally polarized. Γ is the resonance linewidth in the linear regime. Green and gray curves are stable and unstable steady states of a single-mode nonlinear cavity, calculated as explained in Methods. For clarity, measurements at $P = 10$ μW and $P = 100$ μW are multiplied by 20 and 3, respectively, and measurements at $P = 100$ μW and $P = 1$ mW are displaced vertically by 1 μW and 2 μW, respectively.

and dashed curves correspond to cavity length scans whereby the frequency detuning Δ between the laser and the $\ell = 0$ H-polarized resonance increases and decreases, respectively. For $P = 10$ μW we observe a Lorentzian lineshape characterizing the linear regime. Around $P = 100$ μW the resonance bends and displays a small hysteresis. This intensity-induced lineshape asymmetry is due to $CsPbBr_3$ having a nonlinear refractive index n_2, which we know is negative because the resonance bends towards positive Δ. For $P = 1$ mW the hysteresis widens and we observe optical bistability: two stable states with different intensity at a single driving condition. This is the first observation of optical bistability, the hallmark of a CW nonlinearity, in a HP.

Bistability – the existence of two attractors in phase space – is a property of the system. It exists for certain combinations of laser amplitude and laser-cavity detuning, as Supplementary Figure S4 shows. It does not depend on the way that region of parameter space is accessed. Optical bistability can be revealed in two complementary ways to our detuning scan: by scanning the laser power (see Supplementary Figure S5), or by letting the noise reveal the existence of two attractors in the system's dynamics under constant driving (see Supplementary Figure S6).

Polarization rotation and multistability

We now return to diagonally polarized driving, and probe the interplay of nonlinearity and polarization in our cavity. Figures 3(a) and 3(b) show polarization-resolved transmission spectra in the linear and nonlinear regime, respectively. In the linear regime, the V-polarized resonance has lower amplitude than the H-polarized resonance. While the incident polarization axis is exactly midway between the V and H crystal axes, the spatial overlap of the incident Gaussian beam with the modes is different. The overlap is smaller with the 'd'-like mode profile of the V-polarized resonance, resulting in its lower excitation efficiency. In the nonlinear regime obtained for $P = 5$ mW, Fig. 3(b) shows optical hysteresis and bistability. Notice the power rise in V polarization shortly after the power drop in H polarization around $\Delta/\Gamma = 9$. This behavior, only observed when both modes are driven via an incident polarization that is not parallel to the H or V axis (see Supplementary Figure S7), suggests energy transfer between H and V polarization. Such energy transfer is impossible in the linear regime, where the modes are orthogonal and decoupled. However, at sufficiently high intensities the modes couple nonlinearly as explained ahead.

To characterize the output polarization state and its fluctuations, we plot in Fig. 3(c) a histogram of the polarization contrast $(P_H - P_V)/(P_H + P_V)$ spectrum. P_H and P_V are the power in H and V polarization, respectively. Excitation conditions are the same as in Fig. 3(b). The histogram contains 40 trajectories mea-

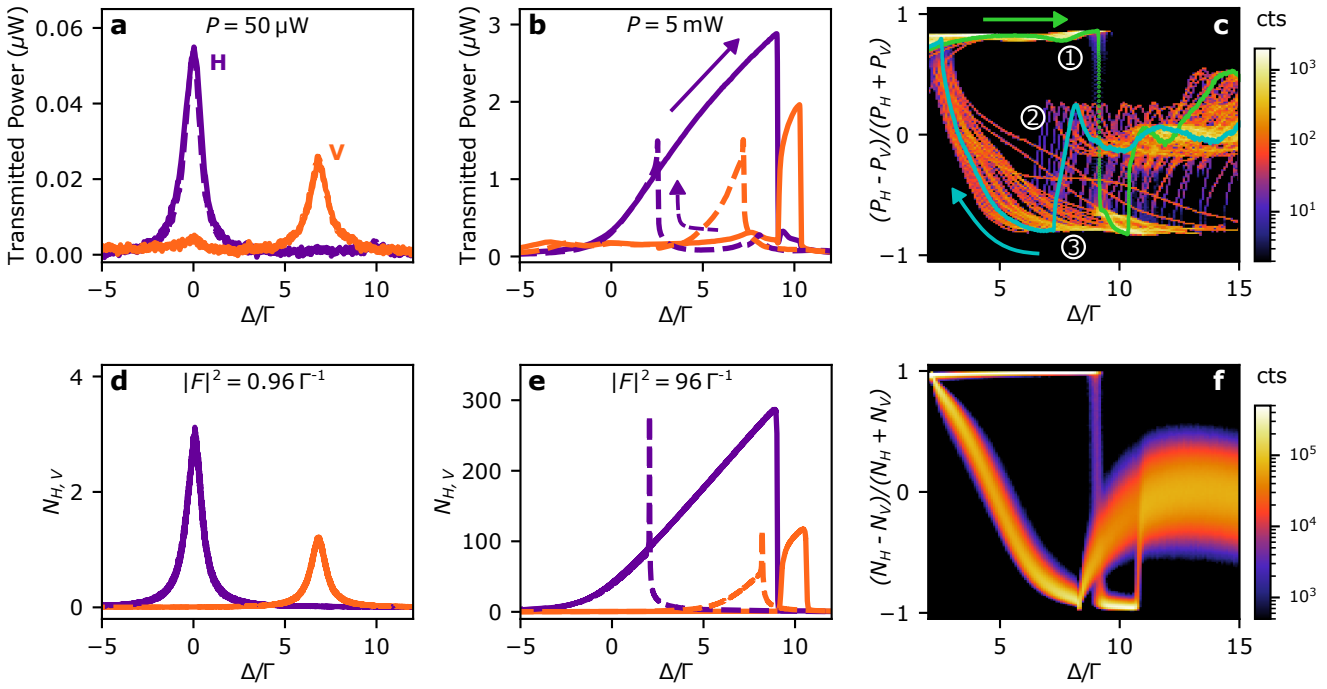

FIG. 3. **Nonlinear polarization rotation and multistability.** Polarization-resolved transmitted power in the (a) linear, and (b) nonlinear, regime obtained by setting the incident power P to the indicated value. The incident laser is diagonally polarized. Purple and orange curves correspond to H and V-polarized detection, respectively. Solid and dashed curves correspond to cavity length scans whereby Δ increases and decreases, respectively. (c) Histogram of the polarization contrast $(P_H - P_V)/(P_H + P_V)$ spectrum for the same driving conditions as in (b). One forward and one backward trajectory are highlighted in green and cyan, respectively. Encircled numbers label states. (d-f) Calculations corresponding to (a-c). The number of intra-cavity polaritons $N_{H,V}$ in (d,e) replaces the experimental transmitted power in (a,b). The histogram in (f) was obtained by calculating the polarization contrast spectrum for 1024 different realizations of the noise.

sured for both increasing and decreasing Δ/Γ; that number is limited by an uncontrolled cavity length drift in our cryostat. Starting in state '1' and increasing Δ/Γ, the polarization state evolves along the green arrow until it rotates from H to V around $\Delta/\Gamma = 9$. The system then settles in state '3', and upon further increasing Δ/Γ it jumps to state '2'. State '2' is detuned from both resonances, and the powers in H and V polarization are therefore equal and low. As a result, state '2' appears broader in Fig. 3(c) than states '1' and '3'; its mean intra-cavity intensity is low, while the noise variance is unchanged.

After reaching the largest Δ/Γ in our protocol, the direction of our cavity length scan is reversed. The polarization state then returns along state '2', jumps down into state '3', and finally rises smoothly to state '1' following the curved arrow in Fig. 3(c). To illustrate this path, we highlight in cyan one trajectory measured in the backward scan. Notice how the jump from state '2' to state '3' in the backward scan (sometimes) occurs at a smaller Δ/Γ than the jump from state '1' to state '3' in the forward scan. This feature is indicative of tristability, i.e., three stable states at a single driving condition. In Supplementary Figure S8 we show, theoretically, that our system is indeed expected to be tristable in this regime. Overall, Fig. 3(c) showcases the potential to fully rotate the polarization state of light leveraging the CW nonlinearity of our $CsPbBr_3$ cavity.

Nonlinear interaction of polarization modes has been achieved in few other experimental platforms, such as GaAs [19] and fibre [20] cavities. Those systems offer a rich playground for exploring functionalities emerging from interacting polarization modes, such as nonreciprocity [33]. In this vein, our results position $CsPbBr_3$ on par with these well-established platforms for nonlinear optics. However, as shown in the remainder of this manuscript, the nonlinearity of our system is unique in its characteristics.

To elucidate the physics of our system and the characteristics of its nonlinearity, we developed a coupled-mode model as explained in Methods. It describes two complex-valued fields, $\alpha_{H,V}$, coherently driven with amplitudes reproducing the resonance amplitudes observed in Fig. 3(a). The frequency detuning between the two modes matches the one observed in Fig. 3(a). In addition, each mode is subject to dissipation, white noise, and two types of interaction. We include a self-interaction proportional to the intensity in the same

mode, and a cross-interaction whereby the intensity in one mode modifies the frequency of the other and vice-versa. The latter is similar to a cross-Kerr nonlinearity [34] or cross-phase modulation [35, 36], albeit the response of our system is non-instantaneous. Figures 3(d-f) show calculations based on our model, reproducing our observations in Figures 3(a-c).

The good agreement between experimental and theoretical spectra depends on several assumptions and constraints in the model that elucidate the properties of our system. First, self-interactions need to be non-instantaneous. Otherwise, the overshoot arising when decreasing Δ (see dashed curve in Fig. 2(c) for largest power) cannot be observed with our limited photodetection bandwidth. Indeed, from the width of that overshoot we deduce a characteristic time for the self-interactions $\tau_s = 4$ μs (see Supplementary Figure S9). Second, cross-interactions also need to be non-instantaneous. Otherwise, the power in V polarization rises abruptly, rather than gradually, after the power drop in H polarization. Supplementary Figure S10 illustrates how theoretical spectra deviate from our experimental observations if self- and cross-interactions are assumed to be instantaneous. Calculations in Supplementary Figure S11 further demonstrate that the cross-interaction time τ_c is similar to τ_s. Third, our model enables to constraint the relative strength of self- and cross-interactions. We find that the two interactions are approximately equally strong. Deviating from this condition by a factor of three or more results in major modifications to the calculated lineshapes (see Supplementary Figure S12).

Signatures of criticality

Recent experiments with $CsPbBr_3$ polaritons at room temperature displayed ultrafast nonlinearities under femtosecond-pulse excitation; these were attributed to polariton-polariton interactions [9, 10, 14]. In contrast, our experiments under CW driving display time-delayed nonlinear effects similar to those observed when an optical mode couples to a thermal field [37–39] or an exciton reservoir [24, 40]. However, unlike any thermo-optical or excitonic nonlinearity that has been reported, the nonlinearity of our $CsPbBr_3$ cavity exhibits an intriguing temperature dependence indicative of critical or near-critical behavior. To evidence this dependence in a minimal configuration, we probe our cavity with H-polarized light and measure the optical hysteresis for variable temperature.

Figure 4(a) shows averaged optical hysteresis measurements at three temperatures T and fixed laser power. Since we probe a single mode and everything besides temperature is unchanged, the larger hysteresis at $T = 62$ K must be due to an enhanced self-interaction strength (U_s in our model, described in Methods). To elucidate the origin of this enhancement, in Fig. 4(b) we plot the hysteresis area [shaded areas in Figure 4(a)] versus temperature. The hysteresis area, and hence U_s, surges as T approaches 65 K from either side. The resonance lineshape bends towards positive detuning for every temperature we probed, meaning the sign of n_2 does not change across 65 K.

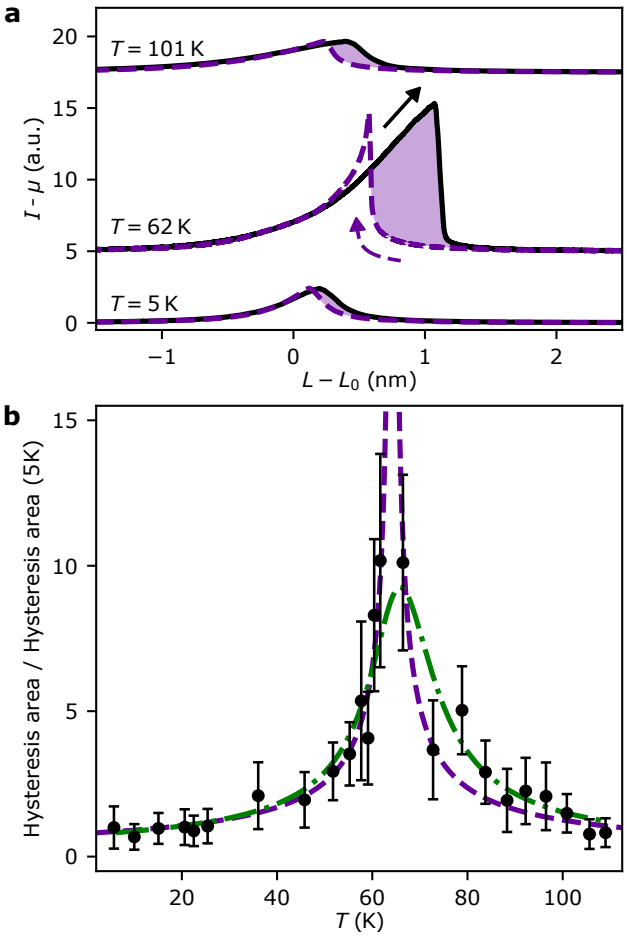

FIG. 4. **Optical hysteresis reveals signatures of a phase transition.** (a) Transmitted intensity, averaged over 50 cycles, for $T = 5$ K, $T = 62$ K, and $T = 101$ K. Solid black and dashed purple curves correspond to an increasing and decreasing cavity length L, respectively; L_0 is the cavity length for which the laser frequency exactly matches the $\ell = 0$ H-polarized resonance frequency. The shaded regions indicate the hysteresis area. The mean of the noise μ was subtracted from the transmitted intensity. For clarity, the $T = 62$ K and $T = 101$ K measurements are displaced vertically. (b) Average hysteresis area, referenced to the area at $T = 5$ K, versus temperature. Dots and errorbars correspond to the mean and standard deviation, respectively, of 50 measurements. Dashed purple curve is a power-law fit to the experimental data. Dash-dotted green curve is obtained from a fifth-order polynomial fit to the integrated hysteresis area, as explained in Supplementary Figure S13. The mean squared residuals of the fits corresponding to first and second order phase transitions are 0.97 and 0.61, respectively. For all measurements, the incident laser was H-polarized, and the power was $P = 600$ μW.

While the microscopic origin of both the CW nonlinearity and its enhancement at a finite temperature

is unclear to us, we suspect that a phase transition in $CsPbBr_3$ may be involved. To assess the plausibility of a first or second order phase transition, we fitted our data with two functions. One (dashed purple curve) fit is a power law of the form $C|T - T_c|^{-\gamma}$, with the constant C, critical temperature T_c, and exponent γ as fit parameters. The divergence at T_c, consistent with our experimental data, is the hallmark of a second order phase transition. The second function we fitted (dash-dotted green curve) corresponds to a first order phase transition, where a finite enhancement of the nonlinearity is expected; the fitting approach for this case is explained in Supplementary Figure S13. While the fit implying a second order phase transition is somewhat better (see figure caption), a first order transition cannot be excluded.

At temperatures above those considered in Fig. 4(b), we observed a significant reduction in transmitted intensity (see Supplementary Figure S14) and thus of the signal-to-noise ratio (SNR). We tentatively attribute this lower SNR to the reduction in quantum efficiency of $CsPbBr_3$ with temperature (see Supplementary Figure S15) [41, 42]. While our experiments involve coherent instead of incoherent driving as in photoluminescence, re-absorption mechanisms degrading the quantum efficiency also degrade the transmission. Our measurements also indicate that the $CsPbBr_3$ CW nonlinearity becomes extremely weak (at best) above 110 K and undetectable at 150 K (see Supplementary Figure S14.) This is consistent with the fact that all room-temperature $CsPbBr_3$ nonlinearities reported to date have required pulsed excitation. Clearly, the CW nonlinearity here studied is of a different origin.

Discussion

To conclude, we discuss two perspectives emerging from our results. One perspective is to clarify the strength and origin of the $CsPbBr_3$ CW nonlinearity. Quantifying the nonlinearity strength is challenging. For GaAs cavities, excitonic nonlinearities spanning nearly 5 orders of magnitude in strength have been reported after 3 decades of research [23]. For $CsPbBr_3$ cavities, excitonic nonlinearities spanning nearly 4 orders of magnitude (~ 0.1 μeV μm^2 [10, 14], 41 μeV μm^2 [6], and 600 μeV μm^2 [13]) have been reported under pulsed excitation alone. The large spread of reported values for a given material reflects the challenges in accurately determining the nonlinearity strength. The challenge is even greater for $CsPbBr_3$ under CW driving, where disentangling contributions of ultrafast excitonic nonlinearities [6, 10, 13, 14] and our ~ 4 μs nonlinearity is difficult. Actually, the same difficulty arises under pulsed excitation if the pulse repetition rate exceeds the ~ 0.25 MHz relaxation rate of the nonlinearity we found. Our work thus opens an interesting new question about the relative strength of different nonlinearities in $CsPbBr_3$. New methods are needed to answer that question.

Establishing the origin of the $CsPbBr_3$ CW nonlinearity is also challenging. We believe thermal effects are the most likely explanation. The microsecond relaxation time we observed, similar for thermo-optical nonlinear cavities [37–39], supports our hypothesis. However, explaining the non-trivial temperature dependence of the nonlinear response requires an additional mechanism. Our intuition, to which we alluded in the previous section, is that a phase transition at 65 K is involved. At a phase transition, the change in refractive index with temperature $\partial n/\partial T$ is maximized [43]. $\partial n/\partial T$ remains finite at a first-order transition, and diverges at a second-order transition. If the nonlinearity is thermal, its strength is given by $\partial n/\partial T$. Therefore, the combination of thermo-optical nonlinearity and a phase transition (of as yet unclear order) can qualitatively explain our entire data set in Fig. 4.

Our interpretation raises important questions. For instance, if the CW nonlinearity is thermal, why has it never been observed at high temperature? In this vein, we highlight that we failed to observe clear signatures of bistability above 110 K. All $CsPbBr_3$ crystals degraded at powers well below any detectable nonlinear threshold at higher temperatures. We believe that this is due to the increased non-radiative losses which also degrade the transmission (see Supplementary Fig. S14 and the discussion around that figure). Another important question emerging from our hypothesis is: What is the nature of the apparent phase transition? Structural phase transitions have been reported for $CsPbBr_3$ [44–46], but only at higher temperatures. Light-induced phase transitions have also been reported for $CsPbBr_3$, but their reported properties are incompatible with our observations. Their relaxation times exceed μs by many orders of magnitude [47, 48], and they result in an intensity dependent birefringence [48]. In contrast, the good experimental-theoretical agreement in Fig. 3 is only obtained by assuming a birefringence independent of power. More generally, a light-induced phase transition cannot explain our results in Fig. 4 obtained at constant laser power; a temperature-induced, not light-induced, transformation is required. In search for other insights, we measured temperature-dependent photoluminescence and absorbance spectra of a bare $CsPbBr_3$ crystal; see Supplementary Figure S16. No clear indications of a phase transition around 65 K were found in that data. Nonetheless, the nonlinear-to-linear response ratio may provide a clearer signature of a phase transition [49]. This could explain why our new experimental approach, characterizing the CW nonlinearity strength in $CsPbBr_3$ as a function of temperature, may be uniquely suited to identify phase transitions that were undetected by other methods. In case a phase transition is confirmed, $CsPbBr_3$ would rise as a particularly interesting platform to realize strongly correlated states of light-matter mixtures [50–52], and to probe the influence its emergent phases (e.g. ferroelectricity [46]) on light and viceversa.

$CsPbBr_3$ hosts a variety of other effects that could

potentially also underlie its CW nonlinearity. For instance, at low temperatures Cs^+ ions displace within the unit cell and generate a dipole moment [53]; this could enhance the nonlinear response. However, the Cs^+ displacement is monotonic with temperature [53], whereas the CW nonlinearity strength sharply peaks around 65 K. Alternatively, self-trapped excitons have been observed in low-temperature $CsPbBr_3$ [54]. Their 0.12 μs decay time at 10 K [54] is somewhat close to the 4 μs relaxation time retrieved from our experiments. However, as the temperature increases, the self-trapped exciton decay time continuously decreases and becomes 30 ns at 100 K [54]. In contrast, the CW nonlinearity relaxation time retrieved from our experiments displays relatively minor changes with temperature; see Supplementary Figure S17. The two time scales are a factor of 300 apart at $T = 100$ K. Another potential explanation involves interactions between polaritons and the so-called exciton reservoir, resulting in a time-delayed nonlinearity identical to the one in our model [24, 40]. However, the 4 μs relaxation time in our experiments significantly exceeds the 5 ns exciton reservoir lifetime in $CsPbBr_3$ [55]. Last but not least, phonons play an important role in $CsPbBr_3$ and HPs in general [56]. These lattice vibrations with temperature-dependent population can couple to polaritons and form polarons [57], which have been associated with enhanced nonlinearities in HPs [58]. This is an interesting explanation which, like all others given above, only future experiments and modeling will be able to strengthen or rule out.

The second perspective emerging from our results is to use the unique properties of $CsPbBr_3$ (regardless of their microscopic origin) to probe new physics or perform proof-of-principle experiments relevant to applications. In this vein, we discuss next three unique possibilities. First, the combination of CW nonlinearity and birefringence in $CsPbBr_3$ could enable the exploration of spin-orbit coupling physics in strongly interacting regimes. Several experiments with birefringent cavities have recently drwan interest to spin-orbit coupling phenomena [28–30, 32, 59–65]. However, the effects of self-interactions or cross-interactions on such phenomena remain unexplored. Second, $CsPbBr_3$ cavities at low temperature could be used to probe charge transport by polaritons. Although polaritons are charge neutral and generally do not carry electrical current (only exciton currents arise [66]), a significant polariton photocurrent has been predicted in media with broken inversion symmetry [67]. Recent observations of the Rashba effect [45] and ferroelectricity [46] in $CsPbBr_3$ indicate that inversion symmetry can be broken in this material. Since birefringence is generally associated with inversion symmetry breaking, and $CsPbBr_3$ birefrigence depends on temperature (see Supplementary Figure S15), $CsPbBr_3$ cavities are a convenient platform for experiments in this direction. Third, the nonlinear polarization control we demonstrated could be used to realize compact magnet-free nonreciprocal devices. A microsecond nonlinearity is not an obstacle to nonreciprocity and many of its functionalities, as recent experiments have shown [21, 22]. In fact, slow nonlinearities can enable new functionalities such as nonreciprocal pulse compression and reshaping [68].

METHODS

Optical cavity experiments

The planar and concave DBR consist of 10 and 11 pairs, respectively, of alternating layers of SiO_2 and Ta_2O_5. Both DBRs have peak reflectance of 99.9 % at 530 nm. The planar mirror hosts a 280 nm thick $CsPbBr_3$-crystal. We estimated the crystal's thickness by comparing transmission spectra in experiments and transfer matrix calculations; see Supplementary Figure S3. $CsPbBr_3$ has, strictly speaking, a biaxial permittivity tensor [7]: its refractive index is different along all three crystal axes. However, two refractive indices are nearly identical. Due to the way our $CsPbBr_3$ crystal is grown [25], on a mica substrate and subject to lattice matching constraints, two crystal axes with substantially different refractive indices lie in the cavity plane. These different refractive indices result in the birefringence illustrated in Figs. 1 and 2.

For the measurements in Figs. 2(b,c), 3(a-c) and 4, we used a concave mirror with 10 μm diameter and a 25 μm radius of curvature to make a plano-concave cavity. The concave features were made by milling the glass substrate with a focused ion beam prior to DBR deposition [69]. While the typical RMS roughness of our concave mirrors is below 1 nm [69], the roughness is irrelevant because the cavity finesse ($\sim$ 3000) is limited by the mirrors' reflectivities.

The polarization of the incident laser was controlled with a half-wave plate. The cavity transmission was decomposed into orthogonal linear polarizations by a polarizing beam splitter (PBS). The PBS was rotated about the optical axis to ensure its alignment with the crystalline axes of $CsPbBr_3$. For the measurements in Figs. 2(c), 3(a-c), and 4, we modulated the detuning by increasing and subsequently decreasing the mirror spacing at modulation frequency $f_{\mathrm{mod}} = 130$ Hz.

Cryostat and temperature measurements

The cavity is inside a closed-cycle cryostat made by Montana Instruments, model HILA. Supplementary Information Section A includes a detailed description of our cryostat, along with a photo and a technical drawing of our setup in Supplementary Figure S1. The measurements presented in Figs. 1(c-e), 2(b,c) and 3(a-c) were performed with the cryostat base temperature set to 5 K. For the measurements in Fig. 4, we attached a temperature probe to the mirror mount containing the perovksite crystal. This was done to measure the actual sample temperature, which we later found could exceed the cryostat base temperature by 1-2 K. The slightly larger sample temperature is insignificant for the previous results since, as Fig. 4 shows, the nonlinearity strength does not significantly change in the 5-7 K temperature range. Finally, we note that the cryostat pump was temporarily turned off for the measurements in Figs. 1(c,d,e). This was done to minimize the effects of mechanical vibrations. Those vibrations significantly impact our measurements when the cavity length is constant as in Figs. 1(e), or slowly scanned as in Figs. 1(c,d). However, in all other experiments, we circumvent the deleterious effects of vibrations by scanning the cavity length sufficiently fast. In particular, the rate at which we sweep the laser-cavity detuning through the optical resonance is greater than the highest mechanical frequency in our setup.

Cavity length calibration

To estimate the total cavity length, we followed the approach described in Ref. [70]. First, we illuminated the planar part of the cavity and measured the white-light transmission spectrum as a function of the separation between the mirrors. The transmission spectrum displays a series of resonances [see Fig. 1(c) or Supplementary Figure S2], each corresponding to a different longitudinal mode number. Then, we considered the expression for the energy of longitudinal cavity modes: $E_c = hcq/2nL_e$, with h Planck's constant, c the speed of light in vacuum, q the longitudinal mode number, n the refractive index of the intra-cavity medium, and L_e the effective cavity length. This enabled us to determine q and L_e by fitting the expression for E_c to the experimentally observed resonances in the 2.13 - 2.3 eV range. L_e is an effective cavity length because it takes into account the field penetration depth into the DBRs and the optical (rather than physical) thickness of the $CsPbBr_3$ crystal. Otherwise, the above expression would only hold for a cavity made by perfectly conducting metallic mirrors and filled with a homogeneous medium. Through this best-fit approach, we determined that L_e was between 4 μm and 4.5 μm in all our experiments with a plano-concave cavity. The cavity length in those experiments was thus similar to the one in the experiments reported in Fig. 1(c). The half-micron uncertainty in L_e we report is due to the error in the aforementioned fitting approach. This uncertainty is, however, irrelevant to our results. Changing the cavity length by half a micron only changes the power needed for bistability by a few percent. More importantly, all our results remain qualitatively the same.

The horizontal axis in Fig. 1(d) was obtained by subtracting the mean energy $\bar{E}$ of the two resonance peaks from the energy measured with the spectrometer.

To determine the change in cavity length in Fig. 4(a), we used a secondary laser with 632.8 nm wavelength. Since this wavelength is outside the DBR stopband, transmission resonances are broad. This enabled us to measure the transmitted intensity of the secondary laser across a wide range of cavity lengths, and thereby determine the horizontal axis in Fig. 4(a). The relation between the intensity of the secondary laser and the change in cavity length was established using the fact that consecutive longitudinal resonances are half-a-wavelength apart.

Photoluminescence experiments

For the photoluminescence measurements in Figs. 1(e), the cavity was illuminated by a 405 nm CW laser with $P = 100$ μW power. We obtained the dispersion relation by imaging the back focal plane of the collection objective onto the entrance slit of a spectrograph.

Theoretical model

We model our experimental system using coupled integro-differential stochastic equations for complex-valued fields α_H and α_V, corresponding to the $\ell = 0$ H-polarized and $\ell = 2$ V-polarized modes, respectively:

$$\begin{aligned}\dot{\alpha}_H(t) =&\Bigg(i\Delta - \frac{\Gamma}{2} - iU_s\int_0^t ds\ K_s(t-s)|\alpha_H(s)|^2 \\ &- iU_c\int_0^t ds\ K_c(t-s)|\alpha_V(s)|^2\Bigg)\alpha_H(t) \qquad (1a)\\ &+ (1+\rho)[\sqrt{\kappa}F + \frac{D}{\sqrt{2}}\zeta_H(t)]\\ \dot{\alpha}_V(t) =&\Bigg(i\Delta + i\delta - \frac{\Gamma}{2} - iU_s\int_0^t ds\ K_s(t-s)|\alpha_V(s)|^2 \\ &- iU_c\int_0^t ds\ K_c(t-s)|\alpha_H(s)|^2\Bigg)\alpha_V(t)\\ &+ (1-\rho)[\sqrt{\kappa}F + \frac{D}{\sqrt{2}}\zeta_V(t)]. \qquad (1b)\end{aligned}$$

$\Delta = \omega - \omega_0$ is the detuning between the laser frequency ω and the $\ell = 0$ H-polarized resonance frequency ω_0. δ is the frequency difference between the $\ell = 0$ H-polarized and $\ell = 2$ V-polarized resonances. Γ is the total loss rate; we take it to be equal for both modes, as this matches our observations. The non-instantaneous nonlinearities are represented by the terms involving an integral. $K_s(t)$ and $K_c(t)$ are memory kernels for the self- and cross-interactions, respectively. Their properties determine to what extent the past exerts an influence over the future state of the system. U_s and U_c are the self- and cross-interaction strength, respectively. F is the driving laser amplitude and κ is the input-output rate through the mirror on which the laser impinges. ρ is the driving imbalance, determined by the incident laser polarization in our experiments. Note that, even if the incident polarization is diagonal, ρ is non-zero because the overlap of the incident Gaussian beam with the two modes under consideration is different. Finally, $\zeta_{H/V}$ are stochastic processes representing Gaussian white noise in the laser amplitude and phase. They have zero mean, unit variance, and delta correlation. Moreover, all noise sources are uncorrelated. Since $\zeta_{H/V}$ are multiplied by $D/\sqrt{2}$, the standard deviation of the laser noise is D.

We assumed memory kernels of the form $K_s(t) = \exp(t/\tau_s)/\tau_s$ and $K_c(t) = \exp(t/\tau_c)/\tau_c$. These kernel functions are integrable and continuously differentiable. Hence, by defining $w_{s,H/V} = U_s\int_0^t ds\ K_s(t-s)|\alpha_{H/V}(s)|^2$ and $w_{c,H/V} = U_c\int_0^t ds\ K_c(t-s)|\alpha_{V/H}(s)|^2$, we can rewrite Eqs. (1) as a set of ordinary differential equations in a higher dimensional phase space using Leibniz rule, to obtain

$$\begin{aligned}\dot{\alpha}_H(t) =&\left(i\Delta - \frac{\Gamma}{2} - iw_{s,H}(t) - iw_{c,H}(t)\right)\alpha_H(t)\\ &+ (1+\rho)[\sqrt{\kappa}F + \frac{D}{\sqrt{2}}\zeta_H(t)] \qquad (2a)\\ \dot{\alpha}_V(t) =&\left(i\Delta + i\delta - \frac{\Gamma}{2} - iw_{s,V}(t) - iw_{c,V}(t)\right)\alpha_V(t)\\ &+ (1-\rho)[\sqrt{\kappa}F + \frac{D}{\sqrt{2}}\zeta_V(t)] \qquad (2b)\\ \dot{w}_{s,H}(t) =&\frac{1}{\tau_s}\left(U_s|\alpha_H(t)|^2 - w_{s,H}(t)\right) \qquad (2c)\\ \dot{w}_{s,V}(t) =&\frac{1}{\tau_s}\left(U_s|\alpha_V(t)|^2 - w_{s,V}(t)\right) \qquad (2d)\\ \dot{w}_{c,H}(t) =&\frac{1}{\tau_c}\left(U_c|\alpha_V(t)|^2 - w_{c,H}(t)\right) \qquad (2e)\\ \dot{w}_{c,V}(t) =&\frac{1}{\tau_c}\left(U_c|\alpha_H(t)|^2 - w_{c,V}(t)\right). \qquad (2f)\end{aligned}$$

$w_{s,H/V}$ and $w_{c,H/V}$ are real-valued dynamical variables. In the case of thermo-optical cavities, they correspond to a temperature. Here, since we are unsure of the microscopic origin of the nonlinearity in $CsPbBr_3$, we can only state that they represent the degrees of freedom which give memory to the self- and cross-interactions of the modes. τ_s and τ_c are the memory times for the self- and cross-interactions. They are the equivalent to thermal relaxation times in the case of thermo-optical cavities, and to the exciton reservoir lifetime in the case of polariton systems coupled to an exciton reservoir.

We set all model parameters to reproduce our experiments as follows. All model parameters are referenced to Γ, which is the resonance linewidth measured experimentally. Δ is a control parameter, so it is not fixed or constrained. To set the value of κ, we took into account that both mirrors have equal reflectivity and assumed negligible non-radiative losses. The value of ρ was set to reproduce the ratio of peak transmitted powers in the linear regime under diagonally polarized driving [see Fig. 3(a)]. U_s is a free parameter whose exact value is irrelevant. For classical systems like ours, every possible spectral lineshape can be reproduced with any value of U provided that F and Γ are adjusted accordingly. The value of U does not qualitatively change the physics; it only changes the driving amplitude needed to reach a certain nonlinear regime. Therefore, for a given U, it is only relevant to determine the value of $F/\sqrt{\Gamma}$ corresponding to our experiments. We achieved this via the approach described in Ref. [37], referencing F^2/Γ to the laser power needed for optical bistability in experiments.

Calculations were performed by solving Eqs. (2) using the xSPDE Matlab toolbox [71]. From the fields $\alpha_{H/V}$ we computed the number of H and V-polarized polaritons $N_H = |\alpha_H|^2$ and $N_V = |\alpha_V|^2$, respectively. We set $\kappa = \Gamma/2$, $\rho = 0.22$, $\delta = -6.8\Gamma$, $U_s = \Gamma/32$,

$U_c = U_s$, $\tau_s = 150/\Gamma$ and $\tau_c = 1.7\tau_s$ to reproduce our experimental observations. $F = 0.98\ \sqrt{\Gamma}$ in Fig. 3(d), and $F = 9.8\ \sqrt{\Gamma}$ in Figs. 3(e,f). We set $D = 0.025\ \sqrt{\Gamma}$ in Figs. 3(d,e), and $D = 1.25\ \sqrt{\Gamma}$ in Fig. 3(f). The values of τ_s and τ_c in our model deviate significantly from their experimental values, which we deduce as explained in Supplementary Figures S9 and S11. As in Ref. [37], we adjusted their values to avoid unnecessarily long and computationally costly simulations. In particular, simulating a single hysteresis cycle of our experimental system would require a dynamic range of 11 orders of magnitude ($\sim$ 10 fs time step, and $\sim$ ms period). However, by reducing the memory times τ_s and τ_c while respecting the hierarchy of time scales in our system ($\Gamma^{-1} \ll \tau_s \sim \tau_c \ll f_{\mathrm{mod}}^{-1}$ with $1/f_{\mathrm{mod}}$ the modulation period), we obtain good qualitative agreement. Finally, for all dynamical calculations, we took into account the finite bandwidth of our experimental APDs by downsampling numerical data.

Steady states in Fig. 2(c) were calculated by setting the time derivatives in Eqs. (2) to zero and solving for $|\alpha_H|^2$. The stability of the steady states was determined using standard linear stability analysis, i.e. by calculating the eigenvalues of the Jacobian of Eqs. (2).

[1] S. D. Stranks and H. J. Snaith, Metal-halide perovskites for photovoltaic and light-emitting devices, Nat. Nanotechnol. **10**, 391 (2015).

[2] B. R. Sutherland and E. H. Sargent, Perovskite photonic sources, Nat. Photon. **10**, 295 (2016).

[3] S. Makarov, A. Furasova, E. Tiguntseva, A. Hemmetter, A. Berestennikov, A. Pushkarev, A. Zakhidov, and Y. Kivshar, Halide-perovskite resonant nanophotonics, Adv. Opt. Mater. **7**, 1800784 (2019).

[4] R. Su, A. Fieramosca, Q. Zhang, H. S. Nguyen, E. Deleporte, Z. Chen, D. Sanvitto, T. C. H. Liew, and Q. Xiong, Perovskite semiconductors for room-temperature exciton-polaritonics, Nat. Mater. **20**, 1315 (2021).

[5] A. Fieramosca, L. Polimeno, V. Ardizzone, L. D. Marco, M. Pugliese, V. Maiorano, M. D. Giorgi, L. Dominici, G. Gigli, D. Gerace, D. Ballarini, and D. Sanvitto, Two-dimensional hybrid perovskites sustaining strong polariton interactions at room temperature, Sci. Adv. **5**, eaav9967 (2019).

[6] R. Su, J. Wang, J. Zhao, J. Xing, W. Zhao, C. Diederichs, T. C. H. Liew, and Q. Xiong, Room temperature long-range coherent exciton polariton condensate flow in lead halide perovskites, Sci. Adv. **4**, eaau0244 (2018).

[7] W. Bao, X. Liu, F. Xue, F. Zheng, R. Tao, S. Wang, Y. Xia, M. Zhao, J. Kim, S. Yang, Q. Li, Y. Wang, Y. Wang, L.-W. Wang, A. H. MacDonald, and X. Zhang, Observation of Rydberg exciton polaritons and their condensate in a perovskite cavity, Proc. Natl. Acad. Sci. U.S.A. **116**, 20274 (2019).

[8] R. Su, S. Ghosh, J. Wang, S. Liu, C. Diederichs, T. C. H. Liew, and Q. Xiong, Observation of exciton polariton condensation in a perovskite lattice at room temperature, Nat. Phys. **16**, 301 (2020).

[9] R. Tao, K. Peng, L. Haeberlé, Q. Li, D. Jin, G. R. Fleming, S. Kéna-Cohen, X. Zhang, and W. Bao, Halide perovskites enable polaritonic XY spin Hamiltonian at room temperature, Nat. Mater. **21**, 761 (2022).

[10] J. Feng, J. Wang, A. Fieramosca, R. Bao, J. Zhao, R. Su, Y. Peng, T. C. H. Liew, D. Sanvitto, and Q. Xiong, All-optical switching based on interacting exciton polaritons in self-assembled perovskite microwires, Sci. Adv. **7**, eabj6627 (2021).

[11] R. Su, S. Ghosh, T. C. H. Liew, and Q. Xiong, Optical switching of topological phase in a perovskite polariton lattice, Sci. Adv. **7**, eabf8049 (2021).

[12] J. Wu, S. Ghosh, R. Su, A. Fieramosca, T. C. H. Liew, and Q. Xiong, Nonlinear parametric scattering of exciton polaritons in perovskite microcavities, Nano Lett. **21**, 3120 (2021).

[13] J. Wu, R. Su, A. Fieramosca, S. Ghosh, J. Zhao, T. C. H. Liew, and Q. Xiong, Perovskite polariton parametric oscillator, Adv. Photonics **3**, 055003 (2021).

[14] K. Peng, R. Tao, L. Haeberlé, Q. Li, D. Jin, G. R. Fleming, S. Kéna-Cohen, X. Zhang, and W. Bao, Room-temperature polariton quantum fluids in halide perovskites, Nat. Commun. **13**, 7388 (2022).

[15] Y. Zhou, Y. Huang, X. Xu, Z. Fan, J. B. Khurgin, and Q. Xiong, Nonlinear optical properties of halide perovskites and their applications, Appl. Phys. Rev. **7**, 041313 (2020).

[16] D. Sanvitto and S. Kéna-Cohen, The road towards polaritonic devices, Nat. Mater. **15**, 1061 (2016).

[17] I. Carusotto and C. Ciuti, Quantum fluids of light, Rev. Mod. Phys. **85**, 299 (2013).

[18] D. E. Chang, V. Vuletić, and M. D. Lukin, Quantum nonlinear optics—photon by photon, Nat. Photon. **8**, 685 (2014).

[19] T. Paraïso, M. Wouters, Y. Léger, F. Morier-Genoud, and B. Deveaud-Plédran, Multistability of a coherent spin ensemble in a semiconductor microcavity, Nat. Mater. **9**, 655 (2010).

[20] N. Moroney, L. Del Bino, S. Zhang, M. T. M. Woodley, L. Hill, T. Wildi, V. J. Wittwer, T. Südmeyer, G.-L. Oppo, M. R. Vanner, *et al.*, A Kerr polarization controller, Nat. Commun. **13**, 398 (2022).

[21] J. King, C. Wan, T. J. Park, S. Deshpande, Z. Zhang, S. Ramanathan, and M. A. Kats, Electrically tunable VO_2–metal metasurface for mid-infrared switching, limiting and nonlinear isolation, Nat. Photon. **18**, 74 (2024).

[22] M. Cotrufo, A. Cordaro, D. L. Sounas, A. Polman, and A. Alù, Passive bias-free non-reciprocal metasurfaces based on thermally nonlinear quasi-bound states in the continuum, Nat. Photon. **18**, 81 (2024).

[23] E. Estrecho, T. Gao, N. Bobrovska, D. Comber-Todd, M. D. Fraser, M. Steger, K. West, L. N. Pfeiffer, J. Levinsen, M. M. Parish, T. C. H. Liew, M. Matuszewski, D. W. Snoke, A. G. Truscott, and E. A. Ostrovskaya, Direct measurement of polariton-polariton interaction strength in the Thomas-Fermi regime of

exciton-polariton condensation, Phys. Rev. B **100**, 035306 (2019).
[24] D. Schmidt, B. Berger, M. Kahlert, M. Bayer, C. Schneider, S. Höfling, E. S. Sedov, A. V. Kavokin, and M. Aßmann, Tracking dark excitons with exciton polaritons in semiconductor microcavities, Phys. Rev. Lett. **122**, 047403 (2019).
[25] Q. Zhang, R. Su, X. Liu, J. Xing, T. C. Sum, and Q. Xiong, High-quality whispering-gallery-mode lasing from cesium lead halide perovskite nanoplatelets, Adv. Funct. Mater. **26**, 6238 (2016).
[26] D. Biegańska, M. Pieczarka, E. Estrecho, M. Steger, D. W. Snoke, K. West, L. N. Pfeiffer, M. Syperek, A. G. Truscott, and E. A. Ostrovskaya, Collective excitations of exciton-polariton condensates in a synthetic gauge field, Phys. Rev. Lett. **127**, 185301 (2021).
[27] H. Terças, H. Flayac, D. D. Solnyshkov, and G. Malpuech, Non-Abelian gauge fields in photonic cavities and photonic superfluids, Phys. Rev. Lett. **112**, 066402 (2014).
[28] K. Rechcińska, M. Król, R. Mazur, P. Morawiak, R. Mirek, K. Łempicka, W. Bardyszewski, M. Matuszewski, P. Kula, W. Piecek, P. G. Lagoudakis, B. Piętka, and J. Szczytko, Engineering spin-orbit synthetic Hamiltonians in liquid-crystal optical cavities, Science **366**, 727 (2019).
[29] Y. Li, X. Ma, X. Zhai, M. Gao, H. Dai, S. Schumacher, and T. Gao, Manipulating polariton condensates by Rashba-Dresselhaus coupling at room temperature, Nat. Commun. **13**, 3785 (2022).
[30] J. Liang, W. Wen, F. Jin, Y. G. Rubo, T. C. H. Liew, and R. Su, Polariton spin Hall effect in a Rashba-Dresselhaus regime at room temperature, Nat. Photon. **18**, 357 (2024).
[31] A. Gianfrate, O. Bleu, L. Dominici, V. Ardizzone, M. De Giorgi, D. Ballarini, G. Lerario, K. W. West, L. N. Pfeiffer, D. D. Solnyshkov, D. Sanvitto, and G. Malpuech, Measurement of the quantum geometric tensor and of the anomalous Hall drift, Nature **578**, 381 (2020).
[32] Q. Liao, C. Leblanc, J. Ren, F. Li, Y. Li, D. Solnyshkov, G. Malpuech, J. Yao, and H. Fu, Experimental measurement of the divergent quantum metric of an exceptional point, Phys. Rev. Lett. **127**, 107402 (2021).
[33] R. Duggan, J. del Pino, E. Verhagen, and A. Alù, Optomechanically induced birefringence and optomechanically induced Faraday effect, Phys. Rev. Lett. **123**, 023602 (2019).
[34] I.-C. Hoi, A. F. Kockum, T. Palomaki, T. M. Stace, B. Fan, L. Tornberg, S. R. Sathyamoorthy, G. Johansson, P. Delsing, and C. M. Wilson, Giant cross–Kerr effect for propagating microwaves induced by an artificial atom, Phys. Rev. Lett. **111**, 053601 (2013).
[35] V. Venkataraman, K. Saha, and A. L. Gaeta, Phase modulation at the few-photon level for weak-nonlinearity-based quantum computing, Nat. Photon. **7**, 138 (2013).
[36] F. Copie, M. T. M. Woodley, L. Del Bino, J. M. Silver, S. Zhang, and P. Del'Haye, Interplay of polarization and time-reversal symmetry breaking in synchronously pumped ring resonators, Phys. Rev. Lett. **122**, 013905 (2019).
[37] Z. Geng, K. J. H. Peters, A. A. P. Trichet, K. Malmir, R. Kolkowski, J. M. Smith, and S. R. K. Rodriguez, Universal scaling in the dynamic hysteresis, and non-Markovian dynamics, of a tunable optical cavity, Phys. Rev. Lett. **124**, 153603 (2020).
[38] K. J. H. Peters, Z. Geng, K. Malmir, J. M. Smith, and S. R. K. Rodriguez, Extremely broadband stochastic resonance of light and enhanced energy harvesting enabled by memory effects in the nonlinear response, Phys. Rev. Lett. **126**, 213901 (2021).
[39] G. Keijsers, T. Ham, Z. Geng, K. J. H. Peters, M. Wouters, and S. R. K. Rodriguez, Photon superfluidity through dissipation, Phys. Rev. Res. **6**, 023266 (2024).
[40] I. Amelio, A. Minguzzi, M. Richard, and I. Carusotto, Galilean boosts and superfluidity of resonantly driven polariton fluids in the presence of an incoherent reservoir, Phys. Rev. Res. **2**, 023158 (2020).
[41] X. Li, Y. Wu, S. Zhang, B. Cai, Y. Gu, J. Song, and H. Zeng, $CsPbX_3$ quantum dots for lighting and displays: Room-temperature synthesis, photoluminescence superiorities, underlying origins and white light-emitting diodes, Adv. Funct. Mater. **26**, 2435 (2016).
[42] A. Shinde, R. Gahlaut, and S. Mahamuni, Low-temperature photoluminescence studies of $CsPbBr_3$ quantum dots, J. Phys. Chem. C **121**, 14872 (2017).
[43] T. X. Ding, L. Hou, H. v. d. Meer, A. P. Alivisatos, and M. Orrit, Hundreds-fold sensitivity enhancement of photothermal microscopy in near-critical xenon, J. Phys. Chem. Lett. **7**, 2524 (2016).
[44] M. Rodová, J. Brožek, K. Knížek, and K. Nitsch, Phase transitions in ternary caesium lead bromide, J. Therm. Anal. Calorim. **71**, 667 (2003).
[45] M. Isarov, L. Z. Tan, M. I. Bodnarchuk, M. V. Kovalenko, A. M. Rappe, and E. Lifshitz, Rashba effect in a single colloidal $CsPbBr_3$ perovskite nanocrystal detected by magneto-optical measurements, Nano Lett. **17**, 5020 (2017).
[46] X. Li, S. Chen, P.-F. Liu, Y. Zhang, Y. Chen, H.-L. Wang, H. Yuan, and S. Feng, Evidence for ferroelectricity of all-inorganic perovskite $CsPbBr_3$ quantum dots, J. Am. Chem. Soc. **142**, 3316 (2020).
[47] J. Xue, D. Yang, B. Cai, X. Xu, J. Wang, H. Ma, X. Yu, G. Yuan, Y. Zou, J. Song, and H. Zeng, Photon-induced reversible phase transition in $CsPbBr_3$ perovskite, Adv. Funct. Mater. **29**, 1807922 (2019).
[48] P. Cheng, Z. Liu, J. Zhou, R. Kang, X. Wang, X. Li, X. Zhao, J. Zhao, and Z. Zuo, All-optical excitatory and inhibitory synapses based on reversible photo-induced phase transition in single-crystal $CsPbBr_3$ perovskite, Adv. Optical Mater. **12**, 2303306 (2024).
[49] R. Pirc and R. Blinc, Spherical random-bond–random-field model of relaxor ferroelectrics, Phys. Rev. B **60**, 13470 (1999).
[50] O. Cotleţ, S. Zeytinoğlu, M. Sigrist, E. Demler, and A. Imamoğlu, Superconductivity and other collective phenomena in a hybrid Bose-Fermi mixture formed by a polariton condensate and an electron system in two dimensions, Phys. Rev. B **93**, 054510 (2016).
[51] Y. Ashida, A. İmamoğlu, J. Faist, D. Jaksch, A. Cavalleri, and E. Demler, Quantum electrodynamic control of matter: Cavity-enhanced ferroelectric phase transition, Phys. Rev. X **10**, 041027 (2020).
[52] J. Bloch, A. Cavalleri, V. Galitski, M. Hafezi, and A. Rubio, Strongly correlated electron–photon systems, Na-

ture **606**, 41 (2022).
[53] A. Boziki, M. I. Dar, G. Jacopin, M. Grätzel, and U. Rothlisberger, Molecular origin of the asymmetric photoluminescence spectra of $CsPbBr_3$ at low temperature, J. Phys. Chem. Lett. **12**, 2699 (2021).
[54] F. Pan, J. Li, X. Ma, Y. Nie, B. Liu, and H. Ye, Free and self-trapped exciton emission in perovskite $CsPbBr_3$ microcrystals, RSC Adv. **12**, 1035 (2022).
[55] S. Zhang, J. Chen, J. Shi, L. Fu, W. Du, X. Sui, Y. Mi, Z. Jia, F. Liu, J. Shi, X. Wu, N. Tang, Q. Zhang, and X. Liu, Trapped exciton–polariton condensate by spatial confinement in a perovskite microcavity, ACS Photonics **7**, 327 (2020).
[56] Y. Guo, O. Yaffe, T. D. Hull, J. S. Owen, D. R. Reichman, and L. E. Brus, Dynamic emission Stokes shift and liquid-like dielectric solvation of band edge carriers in lead-halide perovskites, Nat. Commun. **10**, 1175 (2019).
[57] D. Ghosh, E. Welch, A. J. Neukirch, A. Zakhidov, and S. Tretiak, Polarons in halide perovskites: A perspective, The Journal of Physical Chemistry Letters **11**, 3271 (2020).
[58] M. A. Masharin, V. A. Shahnazaryan, F. A. Benimetskiy, D. N. Krizhanovskii, I. A. Shelykh, I. V. Iorsh, S. V. Makarov, and A. K. Samusev, Polaron-enhanced polariton nonlinearity in lead halide perovskites, Nano Lett. **22**, 9092 (2022).
[59] C. E. Whittaker, T. Dowling, A. V. Nalitov, A. V. Yulin, B. Royall, E. Clarke, M. S. Skolnick, I. A. Shelykh, and D. N. Krizhanovskii, Optical analogue of Dresselhaus spin-orbit interaction in photonic graphene, Nat. Photon. **15**, 193 (2021).
[60] L. Polimeno, G. Lerario, M. De Giorgi, L. De Marco, L. Dominici, F. Todisco, A. Coriolano, V. Ardizzone, M. Pugliese, C. T. Prontera, V. Maiorano, A. Moliterni, C. Giannini, V. Olieric, G. Gigli, D. Ballarini, Q. Xiong, A. Fieramosca, D. D. Solnyshkov, G. Malpuech, and D. Sanvitto, Tuning of the Berry curvature in 2D perovskite polaritons, Nat. Nanotechnol. **16**, 1349 (2021).
[61] M. Król, K. Rechcińska, H. Sigurdsson, P. Oliwa, R. Mazur, P. Morawiak, W. Piecek, P. Kula, P. G. Lagoudakis, M. Matuszewski, W. Bardyszewski, B. Piętka, and J. Szczytko, Realizing optical persistent spin helix and Stern-Gerlach deflection in an anisotropic liquid crystal microcavity, Phys. Rev. Lett. **127**, 190401 (2021).
[62] M. Muszyński, M. Król, K. Rechcińska, P. Oliwa, M. Kędziora, K. Łempicka-Mirek, R. Mazur, P. Morawiak, W. Piecek, P. Kula, P. G. Lagoudakis, B. Piętka, and J. Szczytko, Realizing persistent-spin-helix lasing in the regime of Rashba-Dresselhaus spin-orbit coupling in a dye-filled liquid-crystal optical microcavity, Phys. Rev. Appl. **17**, 014041 (2022).
[63] J. Ren, Q. Liao, X. Ma, S. Schumacher, J. Yao, and H. Fu, Realization of exciton-mediated optical spin-orbit interaction in organic microcrystalline resonators, Laser Photonics Rev. **16**, 2100252 (2022).
[64] K. Łempicka-Mirek, M. Król, H. Sigurdsson, A. Wincukiewicz, P. Morawiak, R. Mazur, M. Muszyński, W. Piecek, P. Kula, T. Stefaniuk, M. Kamińska, L. De Marco, P. G. Lagoudakis, D. Ballarini, D. Sanvitto, J. Szczytko, and B. Piętka, Electrically tunable Berry curvature and strong light-matter coupling in liquid crystal microcavities with 2D perovskite, Sci. Adv. **8**, eabq7533 (2022).
[65] R. Su, E. Estrecho, D. Biegańska, Y. Huang, M. Wurdack, M. Pieczarka, A. G. Truscott, T. C. H. Liew, E. A. Ostrovskaya, and Q. Xiong, Direct measurement of a non-Hermitian topological invariant in a hybrid light-matter system, Sci. Adv. **7**, eabj8905 (2021).
[66] J. Feist and F. J. Garcia-Vidal, Extraordinary exciton conductance induced by strong coupling, Phys. Rev. Lett. **114**, 196402 (2015).
[67] T. Morimoto and N. Nagaosa, Photocurrent of exciton polaritons, Phys. Rev. B **102**, 235139 (2020).
[68] A. Hofstrand, M. Cotrufo, and A. Alù, Nonreciprocal pulse shaping and chaotic modulation with asymmetric noninstantaneous nonlinear resonators, Phys. Rev. A **104**, 053529 (2021).
[69] A. A. P. Trichet, P. R. Dolan, D. M. Coles, G. M. Hughes, and J. M. Smith, Topographic control of open-access microcavities at the nanometer scale, Opt. Express **23**, 17205 (2015).
[70] Z. Geng, J. Theenhaus, B. K. Patra, J.-Y. Zheng, J. Busink, E. C. Garnett, and S. R. K. Rodriguez, Fano lineshapes and Rabi splittings: Can they be artificially generated or obscured by the numerical aperture?, ACS Photonics **8**, 1271 (2021).
[71] S. Kiesewetter, R. Polkinghorne, B. Opanchuk, and P. D. Drummond, xSPDE: Extensible software for stochastic equations, SoftwareX **5**, 12 (2016).

Data availability

The data in this manuscript will be uploaded to the Zenodo repository before publication.

Acknowledgements

We thank Aurélien Trichet for providing the mirror sample with concave features. We thank Niels Commandeur, Ricardo Struik, and Henk-Jan Boluijt for technical support. We thank Johanna Theenhaus for initial experiments with $CsPbBr_3$ crystals. This work is part of the research programme of the Netherlands Organisation for Scientific Research (NWO). S.R.K.R. acknowledges an ERC Starting Grant with project number 852694.

Author contributions

G.K. and R.M.d.B. performed the experiments. Z.G. and G.K. built the setup. R.M.d.B synthesized the $CsPbBr_3$ crystals. B.V. and K.J.H.P. developed the theoretical model. G.K. contributed to the development of the model, performed calculations, and analyzed all results together with S.R.K.R. S.R.K.R. conceived the project and supervised the work. S.R.K.R. and G.K. wrote the manuscript. All authors discussed the results and the manuscript.

Competing interests

The authors declare no competing interests.